5 = $\frac{D}{2}$

Brookhaven National Laboratory, Upton, New York

Inelastic Neutron Scattering Investigation of Spin Waves and Magnetic Interactions in α-Fe₂O₃[1])

By

E. J. Samuelsen[2]) and G. Shirane

Spin waves in antiferromagnetic α-Fe₂O₃ have been studied at temperatures of 240 and 290 °K by means of inelastic neutron scattering. We report here the first determination of the acoustical branch throughout the entire Brillouin zone and the first observation of the optical branch. The latter shows little dispersion throughout the zone, and has an energy of 1125 °K (97 meV) at the zone centre. At the zone boundaries a gap of 20 to 70 °K exists between the two branches. Heisenberg interaction parameters J_m defined through a Hamiltonian $H = -\sum_{i,j} J_m(r_{ij})\, S_i \cdot S_j$ were obtained through fitting of the data to theoretical expressions for the dispersion relations. The following values were obtained for the first five nearest neighbours: $J_1 = 6.0 \pm 1.6$ °K, $J_2 = 1.6 \pm 0.6$ °K, $J_3 = -29.7 \pm 2.0$ °K, $J_4 = -23.2 \pm 1.0$ °K and $J_5 = -1.0 \pm 1.0$ °K. Interactions to farther neighbours were found to be weak. Neutron intensity data were partly invoked in obtaining the interaction parameters, as two sets of parameters could fit the energy data almost equally well, but they predicted different relative intensities for the two branches in certain regions of the reciprocal space. All spin waves of energy larger than 80 °K, including the entire optical branch, were found to be unaffected by the Morin spin-flip transition at 261 °K temperature. The spin-wave data were used to calculate the sublattice magnetization, the Néel and the Curie-Weiss temperatures, the perpendicular susceptibility at low temperatures and the density of spin-wave state spectrum.

Исследование спиновых волн в антиферромагнитном α-Fe₂O₃ исполнялось с помощью неупругого рассеяния нейтронов при температурах 240 °К и 290 °К. Здесь мы сообщаем первое определение акустической ветви по всей зоне Бриллюэна и обнаруженную нами впервые оптическую ветвь. У последней проявляется небольшая дисперсия по всей зоне при энергии 1125 °К (97 мэв) в центре зоны. На границах зоны между двумя ветвями существует интервал 20 до 70 °К. Параметры взаимодействия Гейзенберга J_m, обозначенные через гамильтониан $H = -\sum_{i,j} J_m(r_{ij})\, S_i \cdot S_j$ были получены методом подгонки данных к теоретическим выражениям для дисперсионных соотношений, и получены следующие значения для первых пяти ближайших соседей: $J_1 = 6.0 \pm 1.6$ °К $J_2 \pm 1.6 \pm 0.6$ °К, $J_3 = -29.7 \pm 2.0$ °К, $J_4 = -23.2 \pm 1.0$ °К, $J_5 = -1.0 \pm 1.0$ °К. Взаимодействия с отдаленными соседями оказались слабыми. Для нахождения параметров взаимодействия частично использовались данные по нейтронным интенсивностям, так как обе группы параметров почти в одинаковой степени соответствуют энергетическим данным, хотя и они предсказывали разные относительные интенсивности для двух ветвей в некоторых областях обратного пространства. Показано, что переход с изменением ориентации спина при температуре 261 °К неоказывает никакого влияния ни на спи-

---

новые волны с энергией свыше 80 К, ни на оптическую ветвь. Расчет под-
решеточной намагниченности, температуры Нелья и Кюри-Вайса, пер-
пендикулярной восприимчивости при низких температурах и плотности спек-
тра состояния спиновых волн производился с помощью данных по спино-
вым волнам.

1. Introduction

As a classical antiferromagnetic material, hematite or α-Fe_2O_3 has been the
subject of numerous studies during the last twenty years. It is readily available
as natural single crystals, recently also as synthetic crystals, it possesses a high
Néel point ($T_N = 960$ °K) and it shows interesting magnetic properties, in
particular that of weak ferromagnetism above the Morin temperature ($T_M =
= 261$ °K). Accordingly, most available measuring techniques have been ap-
plied to it, like neutron diffraction [1 to 3], static magnetic measurements [4 to 9],
AFMR [6, 10 to 11], Mössbauer [12 to 14], NMR [15], ultrasonic attenuation
[16], inelastic neutron scattering [17 to 19]. A reasonably unified picture of the
spin flip at T_M is now emerging [11]. More extensive reference lists to the
α-Fe_2O_3 literature are given in most papers referred to, see for instance [11] and
[14].

Information on the spin-wave dispersion relation and the exchange inter-
actions in α-Fe_2O_3 is still fragmentary, however. Several neutron studies of the
low-energy acoustical spin waves have appeared [17 to 19], but no definite
conclusions on the exchange interactions have been possible from them.

The theoretical expressions for the dispersion relations for spin waves in
corundum type antiferromagnets like Cr_2O_3 and α-Fe_2O_3 were previously derived
by Samuelsen [20]. Since the α-Fe_2O_3 type spin structure makes hematite
a true four-sublattice antiferromagnet, as opposed to Cr_2O_3 which may be describ-
ed by a two-sublattice model, two spin-wave branches should exist for this
material [20]. One objective of the present study was to look for the optical
branch. Another objective was to measure its temperature dependence across
the Morin transition, as a recent calculation by Herbert [21] suggests that the
Morin transition might possibly be driven by a softening of the optical mode.
A third objective was to measure the dispersion relations over a sufficiently
large region of the Brillouin zone to make a determination of exchange interactions
possible. Similar measurements and determinations were recently reported for
Cr_2O_3 [22], and the present work makes an interesting comparison between the
two materials possible. In the final processing of the data, calculations of spin-
wave density of states, sublattice magnetization, Néel and Curie-Weiss tem-
peratures and perpendicular susceptibility were made. The neutron intensity
data were analyzed, and the proper inclusion of the dynamical structure factor
in calculations of neutron peak profiles furnished some help in discriminating
between two possible sets of exchange parameters.

2. The Experiments

2.1 Sample and instrument

The sample used in the present experiments was a natural Elba single crystal
of disk-like shape with diameter 27 mm and thickness 16 mm. Spectrographic
analysis showed the following amounts of impurities present: Sn 0.2%, Zn 0.2%,
Cu 0.05%, Si 0.02%, Mg 0.005%, and Ti < 0.01%.

Fig. 1. The (1$\bar{1}$0)* plane of the reciprocal space. The Brillouin zones are shown around the origin and the three lattice points where most measurements were performed. Filled points indicate magnetic lattice points, open points are purely nuclear. Size of symbols gives a rough measure of static structure factor
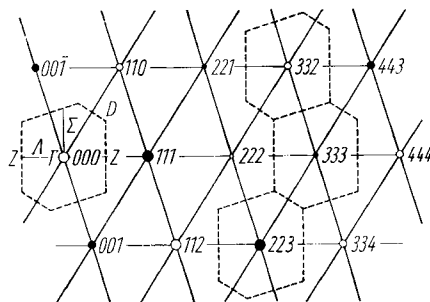
The crystal is imperfect and has a mosaic width of 0.6° and 0.4° measured at the (333) and the (1$\bar{1}$0) rhombohedral reflections, and the rocking curves are slightly asymmetric. It has at least one sizable ($\approx 15\%$ volume) crystallite, misaligned at 48° around [1$\bar{1}$0]. The large mosaic of the crystal prohibited measurements for energies less then 7 meV due to contamination from the Bragg scattering. In particular, it was not possible by neutron scattering to establish the energy gap of the acoustical branch.

The crystal was held in a frame of thin aluminum on the coldfinger of a temperature-controlled liquid nitrogen dewar. Most measurements were performed at 240 °K, which is just below the Morin transition point, T_M, but for checking on the effect of the spin-flip on the neutron scattering some data were taken also at 290 °K.

The measurements were carried out on triple-axis spectrometers at the Brookhaven High Flux Beam Reactor. For an incident neutron energy of 38 meV pyrolytic graphite was used as monochromator and analyzer, and for energies of 100, 160, and 165 meV, Be(110) and Zn(002) were used.

The sample was mounted with its [1$\bar{1}$0] axis vertical, so that the measurements were confined to the (1$\bar{1}$0)* plane only. Fig. 1 shows a part of this plane, with the Brillouin zone (B.Z.) indicated around some of the reciprocal lattice points. Most measurements were taken along the directions [111], [110], and [11$\bar{2}$] at various lattice points. Choice of lattice points is partly determined by intensity considerations and partly by focusing requirements.

2.2 Corrections for instrumental resolution

The finite resolution of the triple-axis spectrometer makes some corrections of the peak positions necessary, in particular in regions where the dispersion relation is steep. The corrections were carried out by means of a computer program previously described [22]. The program essentially simulates the actual triple-axis measurements, based upon some trial dispersion relation $E_s(q)$ and dynamical structure factor $M(\tau)$. If all intensity-determining factors like the monochromator and analyzer efficiencies and the Debye-Waller factor and the magnetic form factor of the sample were accurately known, the program would also be able to reproduce the actual intensities. Some calculated peaks are later compared with observations.

The approximate $E_s(q)$ used in these calculations was based upon the theoretical expressions [20], parameterized by a least squares fitting to the crude spin-wave data.

The observed peak shapes were normally well reproduced by the calculations, and the shift of the peaks from their nominal energy $\hbar\omega$ or wave vector Q indicated the necessary corrections.
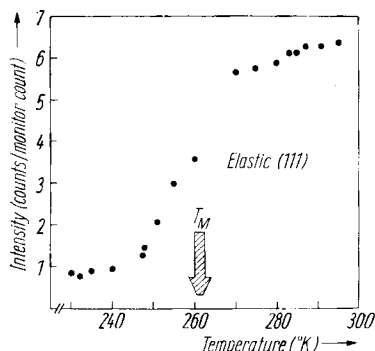
Fig. 2. Measured variation of intensity from (111) with temperature. The spin direction is along [111] at low temperatures, normal to [111] at high temperature. Remnant scattering indicates that the spin-flip is not complete in the crystal used

2.3 Temperature effects

Due to the spin-flip from along [111] below, to normal to [111] above T_M [1], the intensity of magnetic scattering changes grossly by changing the temperature from 240 to 290 °K, since it depends upon the angle α between the spin direction and the scattering vector. The Morin temperature T_M of our crystal was established by following the intensity of the (111) elastic peak, as shown in Fig. 2. The transition is seen to be 25 to 30 °K wide, centred around $T_M = 261$ °K. Since the elastic scattering depends on α through $1 - \cos^2 \alpha$ [1 to 3], remnant intensity shows that the spin-flip is not quite complete at 240 °K. Spin-wave and phonon scattering were distinguished from one another by the effect of the spin-flip on the spin-wave intensity, which depends on α through $1 + \cos^2 \alpha$ [17]. Some peaks measured at 240 and 290 °K are shown in Fig. 3. As expected, spin-wave scattering near the (333), (223) and (332) reciprocal lattice points has higher intensity at 240 °K whereas scattering at (11$\bar{1}$) is more intense at 290 °K and phonon scattering is unaffected. The spin-wave *energy* is, however, only slightly affected by the temperature change. There may be a 1 % decrease in changing the temperature from 240 to 290 °K, which is accounted for by the expected temperature renormalization, usually following the sublattice magnetization. In particular, the optical spin-wave energy shows no tendency for any notable change in crossing T_M. This finding throws doubt on the Herbert mechanism [21] for the Morin transition. Herbert's suggestion was based on the assumption that the exchange part of the optical energy be small, due to possible cancelling. The high optical energy observed shows that this assumption does not hold.

3. Results of Measurements

3.1 The spin wave dispersion relation

The theoretical expression of the spin-wave dispersion relation $E_s(\boldsymbol{q})$ in corundum type antiferromagnets has previously been given [20], based upon a Heisenberg Hamiltonian involving an effective anisotropy field H_A and isotropic exchange interactions J_m, where $m = (1, M)$ labels the M nearest neighbours according to increasing interionic distance. Tables to further identify the J_m's are given elsewhere [20, 22]. Only the case $M = 4$ was considered, but extension to farther neighbours is straightforward. The relations for α-Fe_2O_3 read

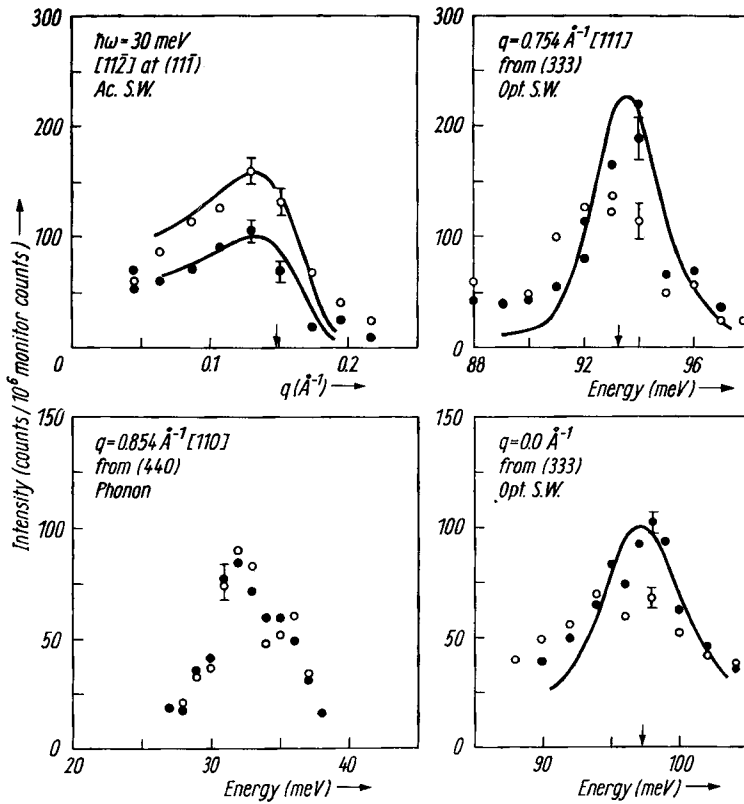$$E_{ac}(\boldsymbol{q}) = P - \sqrt{R} \tag{1}$$

Fig. 3. Some neutron peaks measured at 240 °K (filled symbols) and 290 °K (open symbols) temperature. Intensity of spin-wave peaks changes due to the spin flip. Peak positions are very little affected, also for the optical branch. Calculated peaks are shown, individually normalized to the observed peaks. The arrows indicate nominal momentum or energies
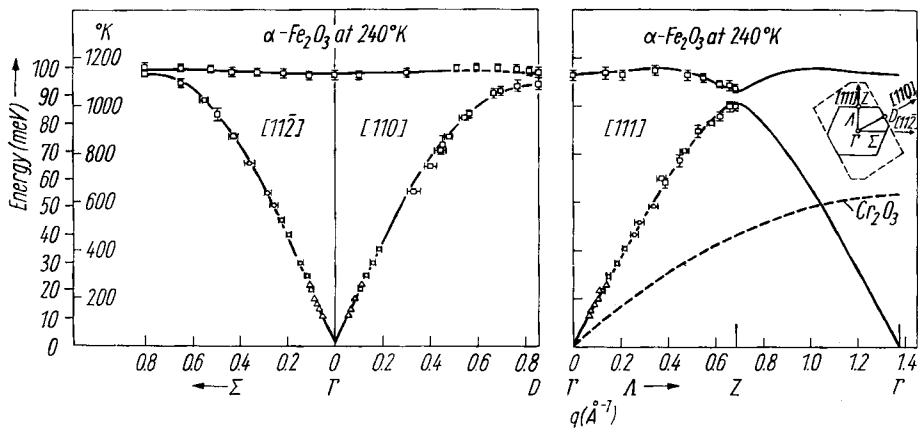
Fig. 4. Most of the observed spin-wave energies in three principal directions after instrumental corrections, shown graphically with the calculated dispersion relations using set (1) of Table 3. Along [111] the calculated curve is shown all to the next zone centre to compare with the dispersion relation of Cr₂O₃ at 78 °K [22], shown as a dashed curve. A sketch of the Brillouin zone is shown inserted in the upper right corner, together with that used for Cr₂O₃ (dashed)

Table 1

Comparison of various determinations of the slopes of the linear part of the acoustical dispersion relation in two principal directions, expressed as spin-wave velocities

Investigation	Reference	Origin of sample	Temperature (°K)	Velocities (km/s)		
				$\parallel$ [111]	$\perp$ [111]	
				$v_{\parallel}$	$v_{\perp}$	$\Delta = \dfrac{v_{\parallel}^2 - v_{\perp}^2}{v_{\parallel}^2}$
Riste and Wanic	[17]	Elba, Italy	295	—	38	—
Dimitrijevic et al.	[18]	Shabry, USSR	295	25 ± 1	30 ± 0.6	−0.31
Samuelsen	[19]	Kragerø, Norway	295	22 ± 2	30 ± 1	−0.47
Randers	[25]	Kragerø, Norway	295	22.4 ± 0.7	28.6 ± 0.3	−0.39
Present work	—	Elba, Italy	240	24.0 ± 0.4	31.6 ± 0.5	−0.42

for the acoustical branch, and

$$E_{\mathrm{opt}}(\boldsymbol{q}) = P + \sqrt{R} \qquad (2)$$

for the optical branch, where P and R are functions of the wavevector $\boldsymbol{q}$ as explained in the Appendix. The relations shown there are similar to those previously given for Cr_2O_3 [22].

The $E_s(\boldsymbol{q})$ relations as determined experimentally at 240 °K are shown graphically in Fig. 4. The slope of the acoustical branch for small q-values is in good agreement with previous determinations. Table 1 shows the values of these slopes from various determinations, expressed in spin-wave propagation velocities.

The optical branch has not been previously observed, although there have been made attempts to locate it [19]. As it turns out to be of such a high energy, however, it could only be found by means of a high flux reactor.

The optical branch is quite flat at energies between 97 and 100 meV (1125 and 1160 °K) except near the zone boundary in the [111] direction, where it dips down to 92 meV (1070 °K). The acoustical branch has an unusual shape in this same region in that its slope is high to within a very short distance from the zone boundary. It may be instructive to compare the spin-wave spectrum in the [111] direction for Cr_2O_3 and $\alpha\text{-}Fe_2O_3$. For Cr_2O_3 an extended zone scheme was found useful [22], corresponding to a small unit cell of the spin structure containing only two Cr^{3+} ions, and only one continuous spin-wave branch was observed within the extended zone. Transferred to a $\alpha\text{-}Fe_2O_3$ zone scheme, this way of presenting the data corresponds to visualizing the acoustical branch of one zone to continue into the optical branch of the neighbouring zone. Since the magnetic repetition distance for $\alpha\text{-}Fe_2O_3$ is twice that of Cr_2O_3 in the direct space along [111], the continuity is, however, broken for $\alpha\text{-}Fe_2O_3$ and a gap is created. This quasicontinuity across the zone boundary is also borne out by the neutron intensities, discussed below. The effect is similar to that found for phonons in comparing the dispersion relation of Na and of ordered β-CuZn [23], both having a b.c.c. structure, but with a double periodicity for β-CuZn. The B.Z. of β-CuZn is thus half that for Na, and what are the dispersion relations

Fig. 5. Density of spin-wave states $\varrho(E)$ calculated by sampling 167192 points within 1/12 of the three-dimensional Brillouin zone into energy boxes of width 2.9 °K, using set (1) of Table 3 to parameterize $E_s(\boldsymbol{q})$
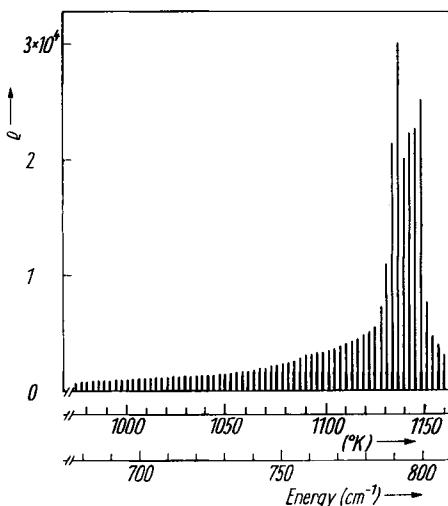
for the acoustical phonons in Na are broken up into acoustical parts in one small zone and optical parts in the neighbouring zones for β-CuZn, with small energy gaps at the new zone boundaries.

The density of spin-wave states was calculated using set (1) of Table 3 for the exchange parameters to parameterize the dispersion relation for sampling over the entire B.Z. Part of the density of states curve is shown in Fig. 5. As already described in Section 2.3 the spin-wave energy was affected very little by the Morin transition at 261 °K.

Some phonons were observed along three symmetry directions, and their initial energy slopes were found to be in agreement with ultrasonic measurements by Shapira [16].

3.2 Neutron intensities

The dynamical structure factor $M(\boldsymbol{\tau})$ for scattering of neutrons by spin waves contains in principle information on the modes of spin precession within the unit cell, and the measured intensities may thus furnish some additional information on the interaction involved between the spins. $|M(\boldsymbol{\tau})|^2$ for α-Fe$_2$O$_3$ in the limit of small $\boldsymbol{q}$ was derived by Samuelsen [20]. The analytical expressions for general $\boldsymbol{q}$ would
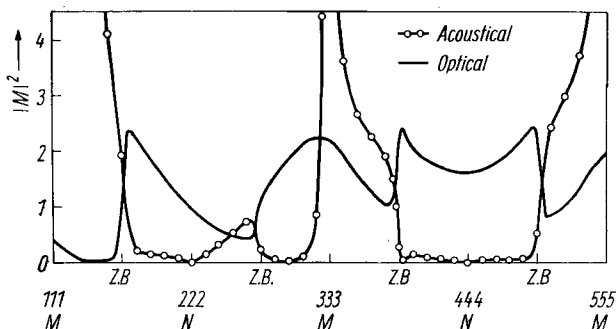
Fig. 6. $|M(\boldsymbol{\tau})|^2$, dynamical structure factors squared calculated with set (1) of Table 3 along [111]. M and N indicate magnetic and nuclear lattice points, respectively

Table 2

Comparison of intensity calculations with observations. Set (1) and set (2) refer to Table 3. Since peak shapes and widths calculated were always in agreement with observations, only peak positions and heights are compared. There is a scaling factor of 0.8 involved between intensities of this table and Fig. 7. The peak positions need not correspond to the spin-wave energies of Fig. 4 because instrumental effects sometimes shift the peaks. The rejection of set (2) is based on the intensities for (0.6; 0.6; 0.4) at (333) and for the three points near and on the Z-point at (223)

Zone	Location in zone	$\|q\|$ (Å)$^{-1}$	Direction [ξηζ]	Peak position (meV)				Peak intensity				Mode	Remark
				Set (1)	Set (2)	Obs	ΔObs	Set (1)	Set (2)	Obs	Δ Obs		
333	0.0; 0.0; 0.0	0.0	—	97.3	96.9	97.0	1.0	96	95	75	10	opt	
	0.45; 0.45; 0.45	0.618	[111]	84.0	84.0	84.0	1.0	49	92	96	10	ac	
	0.45; 0.45; 0.45	0.618	[111]	(93)	(93)	(93)	*	15	2	25	10	opt	* very broad
	0.48; 0.48; 0.48	0.660	[111]	86.7	86.7	86.5	1.0	40	80	70	20	ac	Fig. 7
	0.48; 0.48; 0.48	0.660	[111]	90.4	90.2	91.0	1.0	55	34	65	10	opt + ac	Fig. 7
	0.5; 0.5; 0.5	0.686	[111]	88.0	86.0	88.0	1.5	27	57	88	30	ac	
	0.5; 0.5; 0.5	0.686	[111]	91.6	90.6	92.0	1.5	57	47	85	20	opt + ac	
	0.55; 0.55; 0.55	0.755	[111]	(84)	(84)	—	*	2	6	25	10	ac	* very broad
	0.55; 0.55; 0.55	0.755	[111]	93.5	93.3	93.8	0.5	83	49	175	20	opt	
	0.5; 0.5; 0.0	0.854	[110]	94.0	92.5	94.0	1.0	60	60	100	30	ac	
	0.6; 0.6; 0.4	0.786	[332]	91.0	90.0	—	*	8	60	5	10	ac	* no peak
	0.6; 0.6; 0.4	0.786	[332]	95.0	95.0	95.0	1.5	67	29	50	20	opt	

332	0.0; 0.0; 0.0	0.0	—	97.0	97.0	96.5	1.5	59	59	48	10	opt	
	0.48; 0.48; 0.48	0.660	[111]	86.0	86.0	86.0	1.5	31	31	40	10	ac	Fig. 7
	0.48; 0.48; 0.48	0.660	[111]	92.0	92.0	92.5	1.5	41	41	47	15	opt	Fig. 7
	0.52; 0.52; 0.52	0.713	[111]	85.5	85.5	86.0	1.0	45	45	65	10	ac	Fig. 7
	0.52; 0.52; 0.52	0.713	[111]	93.0	93.0	94.0	1.5	25	25	35	10	opt	Fig. 7
	0.075; 0.075; −0.15	0.324	[112]	97.6	97.7	98.2	1.0	54	54	50	5	opt	
	0.15; 0.15; −0.30	0.649	[112]	98.4	100.0	99.0	1.0	68	86	71	10	opt	
	0.185; 0.185; −0.37	0.800	[112]	97.5 **	100.4	99.0	*	36	48	40	10	opt + ac	* broad ** mainly ac
	0.0; 0.0; 0.5	0.756	[001]	98.5	98.8	100.2	1.5	100	100	85	10	ac	
	0.5; 0.5; 0.0	0.854	[110]	98.3	101.0	98.0	2.5	31	31	35	10	opt	
223	0.45; 0.45; 0.45	0.618	[111]	84.6	83.6	83.7	1.0	123	66	130	15	ac	* broad
	0.45; 0.45; 0.45	0.618	[111]	90.2	90.2	90.0	*	20	40	25	10	opt	* broad
	0.5; 0.5; 0.5	0.686	[111]	87.0	86.6	86.0	1.0	107	48	120	20	ac	Fig. 7
	0.5; 0.5; 0.5	0.686	[111]	92.2	91.9	92.0	1.5	67	118	55	15	opt	Fig. 7
	0.55; 0.55; 0.55	0.755	[111]	89.0	88.0	88.0	*	40	5	50	25	ac	* broad
	0.55; 0.55; 0.55	0.755	[111]	94.2	94.0	93.5	*	84	140	50	20	opt	* broad
	0.33; 0.33; 0.0	0.564	[110]	85.5	85.5	85.2	1.0	220	195	188	30	ac	
	0.5; 0.5; 0.0	0.854	[110]	97.0	100.0	97.8	1.0	128	90	106	15	opt + ac	

be very cumbersome to derive, but when the interaction parameters are known, numerical calculations of $|M(\tau)|^2$ are easily performed. Fig. 6 shows such a calculation along the 111 reciprocal lattice row. The previously determined formulas [20] are well obeyed in the neighbourhood of the reciprocal lattice points. The acoustical intensity gets very large at the magnetic reciprocal lattice points, due to the $1/E(q)$ dependence, and vanishes at the nuclear lattice points for vanishing H_A.

The very abrupt variation of $|M(\tau)|^2$ near the zone boundaries will be noticed for the [111] direction. Similar effects, but less sharp, are found near other zone boundaries. This phenomenon is related to the quasicontinuity between the acoustical branch and the optical branch across the zone boundary, as already discussed. In fact, if the quantity G of equation (4) were zero, $|M(\tau)|^2$ would drop discontinuously to zero at the [111] zone boundary, but such that $|M(\tau)_{ac}|^2$ of one side would continue into $|M(\tau)_{opt}|^2$ of the other side.

Some observed and calculated peak profiles are shown in Fig. 7 for spin waves near the zone boundaries. The calculations were performed using the folding program previously described [22], with the dynamical structure factor
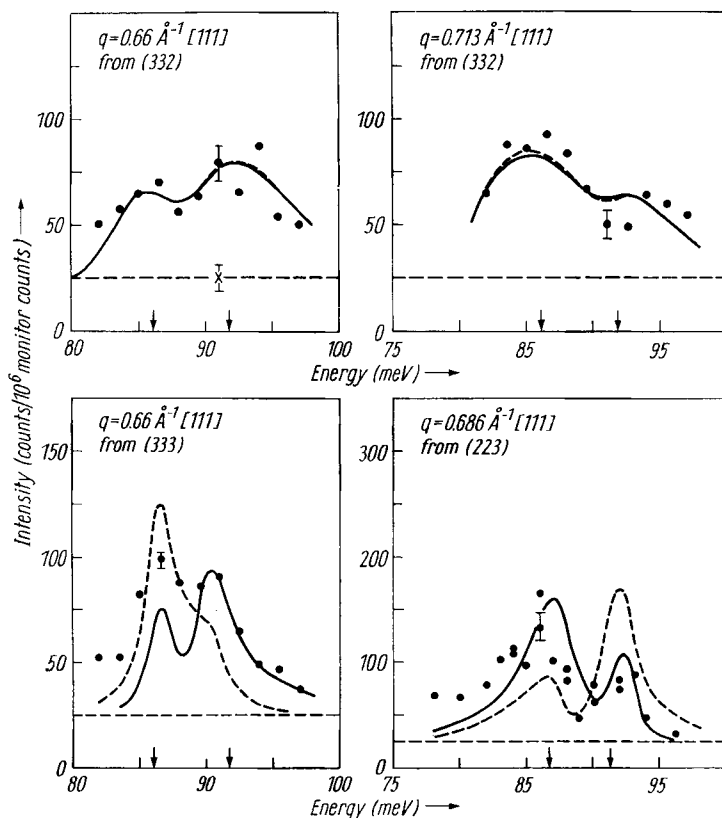

Fig. 7. Observed and calculated neutron peaks near point Z where acoustical and optical spin waves are simultaneously observed. The same background level is assumed for all measured peaks. Full curve is for set (1) of Table 3, dashed curve for set (2). There is only one common scale factor involved, multiplying the peak heights of Table 2 by 1.25

Table 3

Exchange interaction parameters J_m in °K as obtained from least square fits to the observed dispersion relations. F gives the value of the function being minimized [22]. As explained in the text, set (2) was ruled out, based on intensity arguments. "Probable values" are loose averages of the three remaining fits. The ΔJ_m values are those given directly by the least-square program and "uncertainties" are estimated from them

Set of fitting	N		J_1	J_2	J_3	J_4	J_5	J_6	J_7	J_8	J_9	J_{10}	F	Remarks
1	5	J_m:	5.71	0.98	−31.7	−23.3	−1.96						0.646	
		ΔJ_m:	0.79	0.25	0.62	0.33	0.39							
2*	5	J_m:	2.66	−1.32	−34.5	−22.4	0.13						0.683	* Ruled out, see text
		ΔJ_m:	0.78	0.22	0.60	0.35	0.39							
3	7	J_m:	5.20	1.97	−27.7	−24.0	−0.40	0.64	−0.27				0.537	
		ΔJ_m:	0.80	0.31	1.30	0.65	0.51	0.14	0.20					
4	10	J_m:	6.81	2.27	−28.0	−23.0	0.21	0.83	−0.05	−0.53	−0.15	0.0	0.520	
		ΔJ_m:	1.6	0.6	1.5	0.9	0.56	0.35	0.23	0.23	0.20	0.2		
Probable values J_m:			6.0	1.6	−29.7	−23.2	−1.0	0.5	−0.1	−0.3	−0.1	0.0	(0.558)	
Uncertainties ΔJ_m:			1.6	0.6	2.0	1.0	1.0	0.4	0.2	0.3	0.2	0.2		

properly included. Rapid change of the relative intensities in crossing the zone
boundary is demonstrated at the (332) lattice point, and at (333) and (223)
a distinction between the first two sets of interaction parameters of Table 3 is
in principle possible, as shown by the calculated curves. Although the peak at
(333) is inconclusive, the one at (223) obviously favours set (1). Several peak
profiles like those shown in Fig. 7 were calculated. Since the experimental peak
shape and width were always well reproduced by the calculations, only the peak
heights need be used for comparison as is presented in Table 2 for several
high-energy spin waves. The calculated values shown there are normalized by
a factor 0.8 relative to Fig. 7, but no internal scaling is involved. Approximate
forms of the magnetic form factor and the Debye-Waller factor were used.

Two features of Table 2 are of particular importance. Firstly, it can be used
to discriminate between the two sets of interaction parameters that turned out to
fit the energy data almost equally well. To our knowledge this is the first pub-
lished spin-wave case where one has been able to extract useful information
directly from the intensity data. Secondly, Table 2 shows that at least qualita-
tively there is good agreement between observed and calculated variation of
intensity between the various points of the reciprocal space, indicating that
the modes of spin motion implied by the linear spin-wave theory are essentially
correct. For phonons one has been able to go in the reverse direction and deter-
mine the modes of vibration from neutron intensities [24]. For acoustical spin
waves in α-Fe_2O_3, Randers [25] in an unpublished thesis work determined the
neutron intensity on an absolute scale by calibration with incoherent vanadium
scattering, and from the expression for the dynamical structure factor for small q
[20] found a value of 0.3 $\pm$ 0.1 for the ratio

$$\varrho = \frac{2 J_4 + J_3 - J_2 - J_5/3}{3 (2 J_4 + J_3) + J_1}. \tag{3}$$

When J_1, J_2, and J_5 are small, ϱ is 0.333 independent of J_3 and J_4. Our five-
parameter fit gives $\varrho = 0.343 \pm 0.02$.

4. Exchange Interactions

4.1 Fitting to the dispersion relation

The exchange interaction constants were obtained from fitting of (1) and (2)
to the observed dispersion relations. The fitting was carried out by a least
squares program previously described [22].

Two slightly different sets of J_m's were obtained when fitted with five param-
eters, as shown in Table 3. In terms of the minimized parameter F there is
only a little preference for set (1) over set (2). The only region explored where
the dispersion relation would be significantly different for the two sets is for
the optical branch near the zone boundary intersecting [110] (point D). The
measurements tend to favour set (1) in this region, in particular at the zone
boundary itself.

It can be shown that within a five-parameter exchange model the gap between
the optical and the acoustical branch at the point Z (zone boundary intersecting
[111]) is determined by the absolute value of

$$G = 4 S (3 J_2 - J_5). \tag{4}$$

The measurements give $|G| = (70 \pm 23)$ °K, and the principal difference between set (1) and set (2) is the sign of G; they correspond to $G > 0$ and $G < 0$ respectively. Neutron intensities in certain regions of the reciprocal space may be used to distinguish between the two sets. Intensity calculations were discussed in detail in the previous section, and it was shown in Table 2 and Fig. 7 that in some cases the two sets predict quite different relative intensities from the acoustical and the optical branch. Comparison with observations show that although for some peaks none of the two sets give good fit, set (1) is favoured in several cases but set (2) never. Based on this evidence we rule out set (2).

Seven- and ten-parameter fits to the data keeping $G > 0$ are also shown in Table 3. The qualitative picture of large negative J_3 and J_4 and smaller positive J_1 and J_2 does not change by increasing the number of fitted parameters, and the interactions to neighbours beyond the fourth are small. Since the actual values vary somewhat with the number of parameters fitted, we have also included in Table 3 some "probable values" and "uncertainties" of the interactions. One should notice that those "probable values" do not form a set of best fit. Rather they represent a loose average of the fitted sets.

4.2 Discussion of exchange interactions

Qualitatively, the exchange interactions of Table 2 are in excellent agreement with predictions by Li [26], Iida [27], and Goodenough [28], who concluded from superexchange considerations that J_3 and/or J_4 be the strongest interactions in α-Fe$_2$O$_3$. This is in contrast to the situation in Cr$_2$O$_3$, where J_3 and J_4 are quite weak and where J_1 and J_2 represent the strongest antiferromagnetic couplings [22]. J_1 and J_2 in α-Fe$_2$O$_3$ are found to be weak, which could be accounted for by larger cation distances in α-Fe$_2$O$_3$, if direct cation–cation exchange is important [28]. But this would not account for their ferromagnetic sign [28, 29]. "Direct exchange" in the Anderson sense [29] between orbitals with vanishing overlap integral is, however, always ferromagnetic, and that mechanism would not enter for Cr$_2$O$_3$ because of the two empty 3d-orbitals of Cr^{3+}. Previously ferromagnetic 90°-interaction is found in MnF$_2$ [30].

In the five-parameter fit, J_5 is very much the same for α-Fe$_2$O$_3$ and Cr$_2$O$_3$, which is physically reasonable. A negative J_5 may further have some bearing on the spin structure of the ilmenites, in particular MnTiO$_3$, possibly also FeTiO$_3$. The ilmenites have a structure similar to the corundum, but every second cation layer is occupied by the non-magnetic Ti^{4+} [31]. J_5 represents the nearest interaction between the magnetic layers, coupling the spins antiferromagnetically.

5. Thermomagnetic Properties

5.1 The sublattice magnetization

The sublattice magnetization $\langle S^z \rangle$ as a function of temperature was calculated using the Green function technique with the random phase approximation RPA, like for Cr$_2$O$_3$ [22]. The spin-wave occupation number Φ [22, 32] for α-Fe$_2$O$_3$ in the absence of an applied field reads

$$\Phi = \frac{1}{4 N_c} \sum_q \left\{ \frac{A + C'}{E_{ac}(q, 0)} \frac{\sinh \left(X_{ac}(q, T) \right)}{\cosh \left(X_{ac}(q, T) \right) - 1} + \right.$$
$$\left. + \frac{A - C'}{E_{opt}(q, 0)} \frac{\sinh \left(X_{opt}(q, T) \right)}{\cosh \left(X_{opt}(q, T) \right) - 1} - 2 \right\} \tag{5}$$
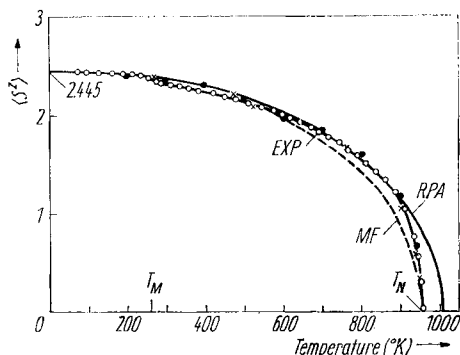
Fig. 8. Calculated sublattice magnetization $\langle S^z \rangle$, zero-point deviation and Néel point T_N, using Green function technique in the RPA with set (1) of Table 3. Mössbauer measurements of the effective hyperfine field by Ono and Ito [12] (●), Freier et al. [13] (×), and van der Woude [14] (—○—○) are normalized to the calculated curve at low T

as can be derived from the general formulation of the RPA [32]. A and C' are defined in the Appendix and

$$X_s(\boldsymbol{q}, T) = \frac{\langle S^z \rangle}{\langle S^z \rangle_{T=0}} \frac{E_s(\boldsymbol{q}, 0)}{k_B T} , \qquad (6)$$

where $E_s(\boldsymbol{q}, 0)$ is the spin-wave energy at zero temperature for the sth branch ($s = \mathrm{ac, opt}$), k_B is the Boltzmann constant, and N_c the total number of unit cells. Then [32]

$$\langle S^z \rangle = S - \Phi + \frac{(2S + 1)\, \Phi^{2S+1}}{(1 + \Phi)^{2S+1} - \Phi^{2S+1}} , \qquad (7)$$

where S is the spin value.

The summation of (5) was performed numerically over $1/12$ of the B.Z. as for Cr_2O_3. The calculated $\langle S^z \rangle$ (using set (1) of Table 3) is shown in Fig. 8 together with the measured hyperfine field H_{eff} by Mössbauer technique [12 to 14]. A value of $\langle S^z \rangle = (2.445 \pm 0.003)\, \mu_B$ is calculated for $T \to 0$, corresponding to a $(2.2 \pm 0.1)\%$ zero-point deviation from the spin-only value of $2.5\, \mu_B$ ($g \approx 2.0$). H_{eff}, having a value of 544 kOe at low temperatures, has been normalized to 2.445 at $T = 0$ in Fig. 8. The abrupt change observed by van der Woude [14] at T_M is due to changes of the orbital and dipolar contribution and is of course not sensed in our calculations. Otherwise, the agreement between calculation and observations is satisfactory up to 900 °K ($T/T_N = 0.94$). Above this temperature, the experimental curve drops quite abruptly to zero at about 960 °K, whereas the theoretical curve continues to a T_N of (1008 ± 4) °K. The abrupt drop of the experimental curve may be related to the lattice parameter changes observed at T_N [33].

5.2 Néel and Curie-Weiss temperatures

T_N was found by means of the RPA as the temperature where $\langle S^z \rangle$ vanishes. The value (1008 ± 4) °K is 5% above the observed value (960 ± 5) °K, where the uncertainty is due to spread in the values among various investigations. A molecular field (MF) calculation gives $T_N = 1340$ °K, which is 40% high. Determination of exchange constants using T_N with MF is therefore highly unreliable. In the spin-wave picture T_N is determined by what amounts to an average of the spin-wave energy over the B.Z. For a great many antiferro-

magnetic materials an empirical relation

$$T_{\mathrm{N}} = \frac{S}{3\,k_{\mathrm{B}}}\,E_{\mathrm{max}} \tag{8}$$

reproduces T_{N} quite well. E_{max} is the maximum energy measured at low temperatures of the spin-wave spectrum, normally corresponding to a zone boundary value. This rule works well for MnF$_2$, FeF$_2$, CoF$_2$, RbMnF$_3$, NiO, Cr$_2$O$_3$, and α-Fe$_2$O$_3$, whose spin-wave spectra have been measured, and it may probably be used as a good first estimate of E_{max} for other antiferromagnets, for instance in connection with light scattering experiments from spin waves.

The existing determinations of the Curie-Weiss temperature θ are from susceptibility measurements at temperatures below 1200 °K. Guillaud [34] found $\theta = 2667$ °K and Cox et al. [35] found $\theta = 1935$ °K. Calculations with set (1) and set (4) of Table 2 using the MF gives

$$\theta = (1300 \pm 58) \text{ °K}$$

and for the perpendicular susceptibility we calculate using the MF

$$\chi_{\perp} = (2.1 \pm 0.1) \times 10^{-5} \text{ erg/G}^2 \text{ g} .$$

Measured values vary between 1.7×10^{-5} and 2.3×10^{-5} erg/G^2 g [5, 6].

6. Conclusion

The main features of the work may be summarized as follows:

a) The entire spin-wave dispersion relation has been investigated. The observation of the optical branch is reported for the first time.

b) The optical branch is unaffected by the Morin transition.

c) Exchange interaction constants were determined. They were found to be entirely different from the corresponding constants in Cr$_2$O$_3$.

d) Neutron intensity data were partly utilized in the determination of the exchange constants.

e) Thermomagnetic quantities calculated using the spin-wave data are in agreement with observations.

Acknowledgement

Appendix

In [20] it is shown that for hematite the dispersion relation reads

$$E(\boldsymbol{q}) = P \pm \sqrt{R} , \tag{A1}$$

where

$$P = A^2 + D\,D^* - B\,B^* - C^2 \tag{A2}$$

and

$$R = 4\,\left(A^2\,D\,D^* + B\,B^*\,(C^2 - D\,D^*) - A\,C\,(B\,D^* + B^*\,D)\right) + {} \\ + (B\,D^* + B^*\,D)^2 . \tag{A3}$$

With an anisotropy field H_{A} and twelve nearest neighbour interactions, the functions involving B, C, and D are identical with those given in [22], and A is

given by

$$A = \mu_B\, g\, H_A + 2\, S\, (-J_1 + 3\, J_2 - 3\, J_3 - 6\, J_4 + J_5 + (6 - 2\, W_c)\, J_6 +$$
$$+ (6 - 2\, V_c)\, J_7 - 6\, J_8 + 3\, J_9 + 3\, J_{10} - 3\, J_{11} - 6\, J_{12})\,. \qquad (A4)$$

C' of equation (5) is defined by

$$C' = \frac{1}{\sqrt{R}}\,[C\,(B\,D^* + B^*\,D) - 2\,A\,D\,D^*]\,. \qquad (A5)$$

References

[1] C. G. Shull, W. A. Strauser, and E. O. Wollan, Phys. Rev. **83**, 333 (1951).
[2] R. Nathans, S. J. Pickart, H. A. Alperin, and P. J. Brown, Phys. Rev. **136**, A1641 (1964).
[3] N. A. Curry, G. B. Johnston, P. J. Besser, and A. H. Morrish, Phil. Mag. **12**, 221 (1965).
[4] F. J. Morin, Phys. Rev. **78**, 819 (1950).
[5] H. Bizette, R. Chevallier, and B. Tsai, C. R. Acad. Sci. (France) **236**, 2043 (1953).
[6] A. Tasaki and S. Iida, J. Phys. Soc. Japan **18**, 1148 (1963).
[7] P. J. Besser and A. H. Morrish, Phys. Letters (Netherlands) **13**, 289 (1964).
[8] P. J. Flanders and J. P. Remeika, Phil. Mag. **11**, 1271 (1965).
[9] G. Cinader, P. J. Flanders, and S. Shtrikman, Phys. Rev. **162**, 419 (1967).
[10] S. Foner and S. J. Williamson, J. appl. Phys. **36**, 1154 (1965).
[11] V. I. Ozhogin and V. G. Shapiro, Zh. eksp. teor. Fiz. **55**, 1737 (1968); Soviet Phys. — J. exper. theor. Phys. **28**, 915 (1969).
[12] K. Ono and A. Ito, J. Phys. Soc. Japan **17**, 1012 (1962).
[13] S. Freier, M. Greensphan, P. Hillmann, and H. Shechter, Phys. Letters (Netherlands) **2**, 191 (1962).
[14] F. van der Woude, phys. stat. sol. **17**, 417 (1966).
[15] D. H. Anderson, Phys. Rev. **151**, 247 (1966).
[16] Y. Shapira, Phys. Rev. **184**, 589 (1969).
[17] T. Riste and A. Wanic, J. Phys. Chem. Solids **17**, 318 (1961).
[18] Z. Dimitrijević, S. Kraśnicki, H. Rzany, J. Todorović, A. Wanic, H. Curien, and A. Milojević, phys. stat. sol. **21**, K163 (1967).
[19] E. J. Samuelsen, Physica (Utrecht) **34**, 241 (1967).
[20] E. J. Samuelsen, Physica (Utrecht) **43**, 353 (1969).
[21] D. C. Herbert, Phys. Rev. Letters **22**, 1184 (1969); J. Phys. C. **3**, 891 (1970).
[22] E. J. Samuelsen, M. T. Hutchings, and G. Shirane, Physica (Utrecht), **48**, 13 (1970).
[23] B. N. Brockhouse, in: Phonons, Scottish Univ. Summer School 1965, Ed. R. W. H. Stevenson, Oliver & Boyd, Edinburgh/London 1966 (p. 139).
[24] J. Harada, J. D. Axe, and G. Shirane, Acta cryst., to be published.
[25] J. Randers, Thesis, University of Oslo, 1969.
[26] Y. Y. Li, Phys. Rev. **102**, 1015 (1956).
[27] S. Iida, J. Phys. Soc. Japan **11**, 1300 (1956).
[28] J. B. Goodenough, Phys. Rev. **117**, 1442 (1960).
[29] P. W. Anderson, in: Magnetism I, Eds. G. Rado and H. Suhl, Academic Press, 1963.
[30] O. Nikotin, P. A. Lindgård, and O. W. Dietrich, J. Phys. C. **2**, 1168 (1969).
[31] J. B. Goodenough and J. J. Stickler, Phys. Rev. **164**, 768 (1967).
[32] R. E. Mills, R. P. Kenan, and F. J. Milford, Phys. Rev. **145**, 704 (1966).
[33] B. T. M. Willis and H. P. Rooksby, Proc. Phys. Soc. (London) **B-65**, 950 (1952).
[34] C. Guillaud, J. Physique **12**, 489 (1951).
[35] D. E. Cox, W. J. Takei, and G. Shirane, J. Phys. Chem. Solids **24**, 405 (1963).